

# Synthesis of $\text{WO}_3$ catalytic powders: evaluation of photocatalytic activity under NUV/visible light irradiation and alkaline reaction pH

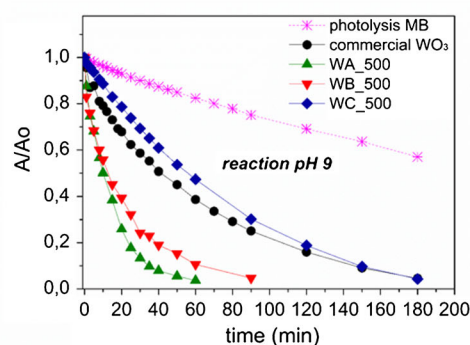
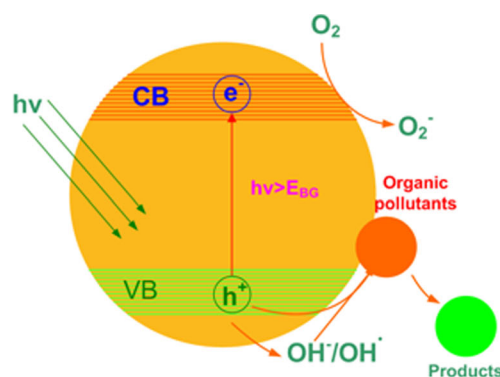
I. Vamvasakis<sup>1</sup> · I. Georgaki<sup>2</sup> · D. Vernardou<sup>2</sup> · G. Kenanakis<sup>2,3</sup> · N. Katsarakis<sup>2,3</sup>

Received: 12 March 2015 / Accepted: 26 May 2015 / Published online: 5 June 2015  
© Springer Science+Business Media New York 2015

**Abstract**  $\text{WO}_3$  catalytic powders were successfully synthesized from tungstic acid and sodium tungstate precursors by simple, low-cost sol–gel and precipitation methods followed by low-temperature hydrothermal treatment.  $\text{WO}_3$  crystallization process was completed with calcination of the samples at 500 and 700 °C. The effects of synthesis method and calcination temperature on the structural, morphological characteristics and surface area

of the samples were investigated. The photocatalytic activity of  $\text{WO}_3$  samples was evaluated by the discoloration efficiency of methylene blue (MB) aqueous solutions under NUV/visible light irradiation at various reaction pH values. The photocatalytic discoloration efficiency of MB was found to increase with increasing reaction pH, with best results obtained at pH 9.

*Graphical Abstract*



✉ I. Vamvasakis  
j.vamvasakis@gmail.com

<sup>1</sup> Department of Materials Science and Technology, University of Crete, 71003 Heraklion, Crete, Greece

<sup>2</sup> Center of Materials Technology and Photonics, School of Applied Technology, Technological Educational Institute of Crete, 71004 Heraklion, Crete, Greece

<sup>3</sup> Institute of Electronic Structure and Laser, FORTH, 71110 Heraklion, Crete, Greece

**Keywords**  $\text{WO}_3$  photocatalytic powders · Sol–gel technique · Acid precipitation technique · Low-temperature hydrothermal treatment · Methylene blue · Alkaline reaction pH

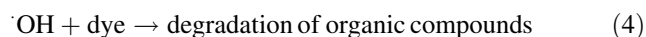
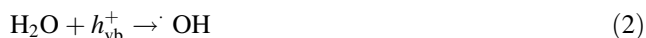
## 1 Introduction

Heterogeneous photocatalysis has proved to be a useful tool for the degradation of water pollutants over the last years. As such, it is been recognized as a green technology

for the treatment of all kinds of contaminants, especially for the removal of organic dyes with complex molecular structure, which are usually present in wastewater from the textile industry [1]. This type of industry consumes large amounts of different dyes, which are lost in quantities of up to 15 % during the dyeing process and disposed of in the textile effluents, leading to a substantial contamination of water [2]. Organic dyes found in textile effluents are a serious ecological problem, since even a small amount of them in water can cause a significant coloring and they can be toxic to aquatic as well as human life [3]. Hence, their removal from wastewater is of fundamental importance for the environment [4].

In view of the economical use of visible light radiation and because of its predominance in the solar spectrum, the development of photocatalysts with high activity under visible light radiation is desirable. In this sense, tungsten trioxide ( $\text{WO}_3$ ) is a visible light responsive photocatalyst that absorbs radiation in the region up to 480 nm [5], which makes it an attractive candidate for photocatalytic applications. Additionally,  $\text{WO}_3$  is a material with high stability in aqueous solution under acidic conditions, and it is an inexpensive material with an  $E_g$  between 2.4 and 2.8 eV [6–8].

The mechanism constituting heterogeneous photocatalytic oxidation processes has been discussed extensively in the literature [9, 10]. Briefly, when a semiconductor absorbs a photon of energy equal to or greater than its band gap, an electron may be promoted from the valence band to the conduction band ( $e_{cb}^-$ ), leaving behind an electron vacancy or “hole” in the valence band ( $h_{vb}^+$ ). Once the charge separation is maintained, the electron and hole may migrate to the catalyst surface where they participate in redox reactions with adsorbed species. Specially,  $h_{vb}^+$  may react with surface-bound  $\text{H}_2\text{O}$  or  $\text{OH}^-$  to produce the hydroxyl radical ( $\cdot\text{OH}$ ) and  $e_{cb}^-$  is picked up by electron-accepting species to generate radical anion, as indicated below.



SC semiconductor, A electron acceptor (generally dissolved oxygen).

It has been suggested that the hydroxyl radicals ( $\cdot\text{OH}$ ) and radical anions are the primary oxidizing species in the photocatalytic oxidation processes. These oxidative reactions would result in the bleaching of the dye or the removal of organic compounds such as pesticides, phenols and other priority organic pollutants.

In this work, we study the synthesis of micro- and nanostructured tungsten trioxide ( $\text{WO}_3$ ) catalytic powders from aqueous solutions of tungstic acid ( $\text{H}_2\text{WO}_4$ ) and sodium tungstate ( $\text{Na}_2\text{WO}_4$ ) precursors and examine the photocatalytic activity of the commercial and synthetic  $\text{WO}_3$  catalysts for the discoloration of aqueous methylene blue (MB) dye solutions in a variety of pH values: 5 (natural pH), 7, 9 and 12.

## 2 Experimental

### 2.1 Material synthesis

For the synthesis of the catalyst powders, simple and environmental friendly sol–gel and deposition–precipitation growth techniques were used, combined with hydrothermal treatments at low temperatures (95 °C), drying of the resultant samples at 110 °C and annealing at 500 or 700 °C.

$\text{WO}_3$  crystalline powders have been synthesized by adopting three different methods:

- A. A thermal treatment method by calcination of tungstic acid  $\text{H}_2\text{WO}_4$  (99 %, Sigma-Aldrich) at 500 or 700 °C for 5 h in a tube furnace (heating rate 5 °C min<sup>−1</sup>, cooling rate 2 °C min<sup>−1</sup>). The samples annealed at 500 and 700 °C will be identified hereafter as WA\_500 and WA\_700, respectively.
- B. A sol–gel method [11], followed by low-temperature hydrothermal treatment. For this purpose, 5-g tungstic acid  $\text{H}_2\text{WO}_4$  (99 %, Sigma-Aldrich) was dissolved in 15.5 ml methanol and the solution was refluxed for 2.5 h at 90 °C followed by slow addition of water (9 ml) until a tungstic acid/water molar ratio = 1:25 was achieved. The solution was kept under stirring for 15 min at room temperature and was further hydrothermally treated at 95 °C for 24 h to obtain hydrated form of  $\text{WO}_3$  ( $\text{WO}_3 \cdot n\text{H}_2\text{O}$ ). The obtained gel was dried in an oven by heating at 110 °C overnight. Dried gels were ground into fine powders and calcined in a tube furnace at 500 °C for 5 h (heating rate 5 °C min<sup>−1</sup>, cooling rate 2 °C min<sup>−1</sup>). The sample annealed at 500 °C will be identified hereafter as WB\_500.
- C. An acid precipitation technique [12, 13] followed by low-temperature hydrothermal treatment. In a typical experiment, 5 g of sodium tungstate dehydrate  $\text{Na}_2\text{WO}_4 \cdot 2\text{H}_2\text{O}$  (99 %, Sigma-Aldrich) was dissolved in 150 ml deionized water to form a transparent solution. Concentrated hydrochloric acid HCl (37 %) was added drop-wise to the solution, until a light yellow tungstic solution was thoroughly formed. The above solution was hydrothermally treated at 95 °C for 24 h to form a

white-yellow precipitate of sodium tungsten oxide hydrate ( $\text{Na}_{0.17}\text{WO}_{3.085}(\text{H}_2\text{O})_{0.17}$ ). The final  $\text{WO}_3$  powder was obtained by centrifugation, drying of the precipitate at 110 °C and further calcination at 500 °C for 5 h (heating rate 5 °C min<sup>-1</sup>, cooling rate 2 °C min<sup>-1</sup>) in a tube furnace. The sample will be identified hereafter as WC\_500.

## 2.2 Characterization of samples

X-ray diffraction patterns were collected on a Panalytical X'Pert Pro MPD diffractometer (45 kV and 40 mA) with Cu  $K\alpha$  X-rays ( $\lambda = 1.5418$  Å) using Bragg–Brentano geometry within the  $2\theta$  range of 20–70°. The crystallite size ( $D$ , in unit of nm) was calculated from peak broadening using Scherrer's equation, which is defined as:

$$D = 0.9\lambda / B \cos \theta \quad (6)$$

where  $\lambda$  is the wavelength of the X-rays (0.15418 nm),  $B$  is the full width at half maximum (FWHM, radian), and  $\theta$  is the Bragg angle (degree).

The surface morphology of the  $\text{WO}_3$  samples was investigated by scanning electron microscopy (SEM) using a JEOL JSM-840 microscope with an accelerating voltage of 20 kV. The specific surface area was measured by means of nitrogen adsorption with a NOVA 3200e volumetric analyzer (Quantachrome, USA) and then calculated by using a Brunauer, Emmett and Tellet (BET) method [14]. The  $\text{N}_2$  adsorption was evaluated at 77 K (−196 °C) after a pretreatment of the sample at 100 °C for 12 h.

Finally, UV–Vis diffuse reflectance spectrums of the samples were obtained by using a UV–Vis spectrophotometer (PerkinElmer, Lambda 950) equipped with an integrating sphere and by using  $\text{BaSO}_4$  as background reference. Diffuse reflectance data were converted to absorption using the Kubelka–Munk function  $\alpha/S = (1-R)^2/(2R)$ , where  $R$  is the measured reflectance, and  $\alpha$ ,  $S$  are the absorption and scattering coefficients, respectively. The energy gap values ( $E_g$ ) were determined with the following relationship:

$$\alpha = A(h\nu - E_g)^n / h\nu \quad (7)$$

where  $\alpha$  is the absorption coefficient calculated from the Kubelka–Munk function,  $h\nu$  is the photon energy,  $E_g$  the energy band gap,  $A$  and  $n$  are constants, and  $n$  has a value of  $n = 1/2$  for materials with direct transition. The optical  $E_g$  of the  $\text{WO}_3$  samples was determined by the extrapolation of the linear portion of  $(\alpha h\nu)^2$  versus  $h\nu$  plots ("Tauc" plots) to the  $x$ -axis, where  $\alpha = 0$ , and, consequently,  $E_g = h\nu$ .

## 2.3 Photocatalytic experiments

The photocatalytic experiments were performed using a cylindrical, thermostated (25 °C), inner lamp-type photoreactor (Heraeus Noblelight GmbH, Hanau-Germany) with a Duran 50<sup>®</sup> borosilicate glass double-walled lamp jacket with a cutoff wavelength at 300 nm ( $\lambda \geq 300$  nm). The reaction mixture was irradiated with a Heraeus TQ 150 Hg lamp with emission range between 240 and 580 nm which was mounted axially in the reactor inside the borosilicate lamp jacket, letting thereby the passing of radiation with maximum fluxes found at  $\lambda_{\text{max}} = 366, 405, 436, 546$  and 577 nm. The photocatalytic activity of  $\text{WO}_3$  samples was evaluated in the discoloration reaction of methylene blue (MB) in aqueous solutions in a variety of pH values: 5 (natural pH), 7, 9 and 12. The pH of the solutions was adjusted by using 1 M NaOH. In all experiments, the  $\text{WO}_3$  powder concentration was 2 g/l and the initial MB concentration was 20 mg/l. In order to ensure that the adsorption–desorption equilibrium of the dye on the catalyst surface had been reached, the solution was kept under magnetic stirring in the dark for 40 min before the light source was turned on. After the lamp was switched on and warmed up for 3 min, 1–2 mL intermediate samples were taken from the reactor at different irradiation time intervals, centrifuged for 1 min and analyzed by a Shimadzu UV\_2401 UV–Vis spectrophotometer between 400 and 800 nm. The absorbance of MB depends linearly on its concentration according to the Lambert–Beer law, so the reduction in MB concentration due to discoloration was determined from the absorbance curves by calculating the area ( $A_t$ ) of each UV–Vis curve with integration limits between 540 and 700 nm and normalized with the initial area ( $A_0$ ) that corresponds to the initial MB concentration. Relative absorbance ( $A_t/A_0$ ) was used as the ordinate in diagrams versus irradiation time, so that the photocatalytic properties of the samples could be compared. Furthermore, for each experiment, the MB discoloration reaction rate constant was calculated from the initial slope obtained by linear regression from a plot of the natural logarithm of the relative absorbance of the dye as a function of irradiation time. The photocatalytic discoloration of MB aqueous solutions with low concentrations can be considered as a pseudo-first-order reaction, and its kinetics can be expressed by the following equation:

$$\ln(A_t/A_0) = -k \cdot t \quad (8)$$

where  $k$  is the apparent rate constant (min<sup>-1</sup>), and  $A_0$  and  $A_t$  are the MB absorbance at  $t = 0$  and  $t = t$ , respectively.

In order to evaluate the mineralization of chemical substances, the total organic carbon (TOC) was analyzed. To determine the TOC removal, 40 ml aliquots were removed from the reactor at various irradiation time

intervals and centrifuged for 10 min at 12,000 rpm to remove the catalyst. The supernatant was finally measured with a Shimadzu TOC-V<sub>SCH</sub> analyzer.

### 3 Results and discussion

#### 3.1 Structure

Typical XRD patterns of the synthesized WO<sub>3</sub> powders and their structural evolution as a function of calcination temperature at 500 and 700 °C are depicted in Fig. 1a, including the XRD pattern of tungstic acid. The structure of tungstic acid (H<sub>2</sub>WO<sub>4</sub>) consisted of layers of WO<sub>6</sub> octahedra which share their equatorial oxygen and water molecules in axial positions and form hydrogen bond with the next layer. Tungsten trioxide (WO<sub>3</sub>), on the other hand, has a monoclinic symmetry with a slight distortion of the cubic ReO<sub>3</sub>-type lattice structure in which corner-sharing distorted and tilted WO<sub>6</sub> octahedron are connected in *x*-, *y*- and *z*- directions, resulting in a three-dimensional structure [15]. A heat treatment leads to the removal of water molecules and formation of WO<sub>3</sub> from tungstic acid, as it is clearly indicated by the change in XRD patterns in Fig. 1a. Crystalline WO<sub>3</sub>, therefore, was obtained after annealing even at 500 °C. The main peaks at  $2\theta = 23.1^\circ$ ,  $23.7^\circ$ , and  $24.4^\circ$  may be ascribed to Miller indices (002), (020), and (200), respectively, in monoclinic WO<sub>3</sub>. The X-ray diffraction patterns of the commercial monoclinic m-WO<sub>3</sub> and the WA\_500, WB\_500 and WC\_500 samples obtained by thermal treatments at 500 °C are shown in Fig. 1b. For the three synthesized samples, all diffraction lines were correctly assigned to the monoclinic polymorph of WO<sub>3</sub> according to the JCPDS Card No. 01-083-0950. Nevertheless, some small differences were observed in the diffraction patterns of the synthesized samples. In particular, for samples WA\_500 and WB\_500, the diffraction line located at  $2\theta = 23.1^\circ$  (*d*<sub>002</sub>) is not formed as well as in samples WC\_500 and commercial m-WO<sub>3</sub>. A similar situation was observed in the group of lines located at around

$2\theta = 33.3^\circ$ – $34.2^\circ$  (*d*<sub>022</sub>, *d*<sub>−202</sub> and *d*<sub>202</sub> diffraction planes). This situation can be associated with the presence of amorphous material at these samples, which produces broad diffraction lines that overlap due to their proximity. Furthermore, for sample WC\_500, two additional diffraction lines appear at  $2\theta = 21.2^\circ$  and  $25.5^\circ$  which most probably correspond to a sodium tungsten oxide phase attributed to sodium impurity from the initial tungsten source and the experimental conditions.

The average crystallite size of the WO<sub>3</sub> samples was determined from the XRD patterns using Scherrer's equation by averaging results from the three main crystallographic directions (002), (020) and (200), and obtained values are listed in Table 1.

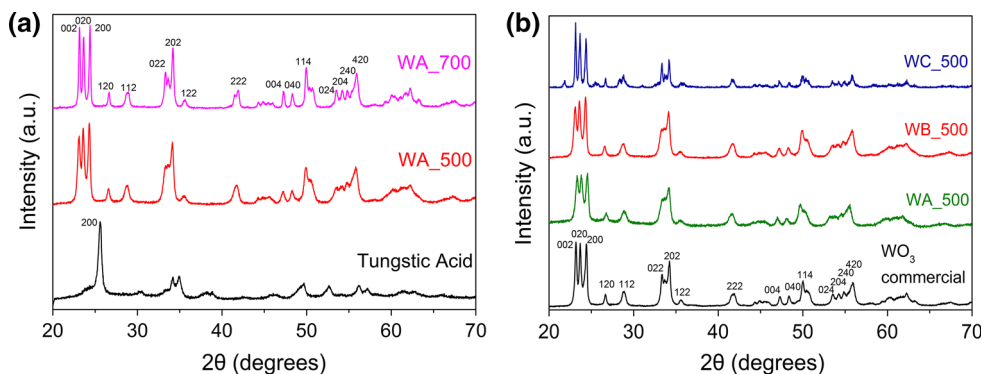
#### 3.2 Morphology and surface area

Figure 2 shows SEM micrographs of the samples WA\_500, WB\_500, WC\_500 and commercial WO<sub>3</sub>. The observed big bulks are due to the agglomeration of smaller particles as confirmed by the crystallite size of the samples that was calculated by the Scherrer's equation, (see Table 1). It is possible to conclude that the annealed samples obtained from tungstic acid (H<sub>2</sub>WO<sub>4</sub>) precursor by the sol-gel method (sample WB\_500) and from direct annealing of H<sub>2</sub>WO<sub>4</sub> at 500 °C (sample WA\_500) consisted of agglomerates of smaller size particles contributing to a porous morphology, as shown in Fig. 2a,b. In contrast, the sample synthesized by the acid precipitation technique

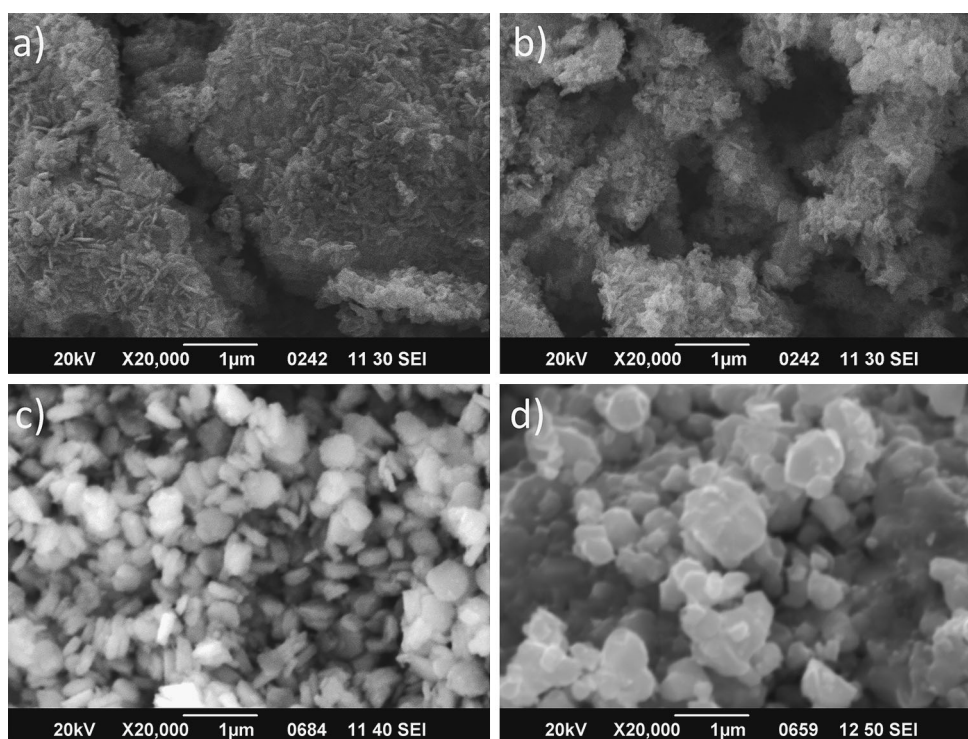
**Table 1** Physical properties of the WO<sub>3</sub> samples synthesized under different experimental conditions

WO <sub>3</sub> sample	Average crystallite size (nm)	BET surface area (m <sup>2</sup> /g)	Band gap <i>E<sub>g</sub></i> (eV)
Commercial	33.6	2.1	2.63
WA_500	19.6	12.1	2.78
WB_500	23.4	11.1	2.76
WC_500	37.7	3.3	2.73

**Fig. 1** **a** Typical X-ray diffraction patterns of tungstic acid and WO<sub>3</sub> samples obtained after calcination for 5 h at 500 and 700 °C. **b** X-ray diffraction patterns of the commercial monoclinic WO<sub>3</sub> and the as-synthesized WO<sub>3</sub> samples calcined at 500 °C



**Fig. 2** SEM images showing the morphology of the  $\text{WO}_3$  samples: **a** WA\_500, **b** WB\_500, **c** WC\_500 and **d** commercial  $\text{WO}_3$



(sample WC\_500) shows the formation of crystal nanoplatelets with sizes varying from 250 to 500 nm (see Fig. 2c), forming larger agglomerates with lower porous morphology resembling more to the morphology of the commercial  $\text{WO}_3$ , which seems to consist of agglomerates of even larger particles, as seen in Fig. 2d.

The BET surface area of the  $\text{WO}_3$  samples is also reported in Table 1. In correspondence with the SEM analysis, the samples with higher porous morphology obtained from  $\text{H}_2\text{WO}_4$  precursor (WA\_500 and WB\_500) exhibit larger surface areas with values in the order of  $11\text{--}12 \pm 0.1 \text{ m}^2/\text{g}$ , while the more crystalline sample WC\_500 obtained from the acid precipitation method from  $\text{Na}_2\text{WO}_4$  precursor shows a BET surface of approximately  $3 \pm 0.3 \text{ m}^2/\text{g}$ , which is similar to the surface area of the commercial  $\text{WO}_3$  powder ( $2 \pm 0.1 \text{ m}^2/\text{g}$ ).

### 3.3 Optical measurements

The optical characteristics of the materials were analyzed by diffuse reflectance ultraviolet–visible/near-IR (UV–vis/NIR) spectroscopy. In Fig. 3a, b, the optical absorption spectra of the  $\text{WO}_3$  samples show absorption onsets associated with electronic transitions in the energy range from 2.63 eV (471 nm) to 2.78 eV (446 nm), indicating an absorption also in the visible light region of the spectra. For comparison, in Fig. 3a, b, the absorption spectra of a well-known photocatalyst  $\text{TiO}_2$  Degussa (P25) nanoparticles

show an absorption onset at 381 nm that corresponds to an  $E_g = 3.25 \text{ eV}$ , indicating that Degussa absorbs light only in the UV region of the spectra.

The  $E_g$  calculated for the commercial  $\text{WO}_3$  was found to be approximately 2.63 eV and an average value of  $E_g = 2.75 \text{ eV}$  was calculated for the synthesized samples, as shown in Table 1. No significant differences in the  $E_g$  values were observed among the synthesized  $\text{WO}_3$  samples which were found to be in agreement with typical values for  $\text{WO}_3$  as mentioned before. In comparison with the commercial  $\text{WO}_3$ , the “blue shift” observed for the synthesized samples may be attributed to their smaller grain size as can be inferred from the SEM analysis.

### 3.4 Photocatalytic activity

The photocatalytic activity of the  $\text{WO}_3$  samples was evaluated in discoloration of MB aqueous solutions in natural pH and at various pH values. Under dark conditions, the adsorption/desorption equilibrium between MB molecules and the surface of the catalysts was achieved after 40 min of reaction time, without observing any significant change in MB concentration. Illumination in the absence of catalyst did not result in any significant discoloration of the MB solution at natural  $\text{pH} \approx 5$ . As can be seen in Fig. 4a, photolysis of MB at natural pH without the use of  $\text{WO}_3$  catalyst displays nonsignificant discoloration ( $\sim 26\%$ ) after 180 min of irradiation, while photocatalytic

discoloration in the presence of commercial  $\text{WO}_3$  and the synthetic samples WA\_500, WB\_500 and WC\_500 exhibits yields of 37, 47, 45 and 43 %, respectively. Although the presence of both light irradiation and  $\text{WO}_3$  catalysts enhances MB discoloration, the photocatalytic activity of the  $\text{WO}_3$  samples at natural pH appears to be considerably low.

The effect of reaction pH was studied in the range of  $\text{pH} \approx 5$  (natural pH), 7, 9 and 12. Photolysis experiments were carried out in order to separately evaluate the effect of pH and irradiation in discoloration of MB solutions. Also, for comparison, the effect of NaOH without irradiation and in the absence of catalyst was examined for the two elevated pH values 9 and 12, since previous works have

suggested that MB decays in the presence of strong alkaline conditions and slowly converts into Bernthsen's methylene violet (MVB) via hydrolysis [16–18]. The results of MB photolysis experiments in the tested pH values and the effect of alkali at  $\text{pH} = 9$  and 12 (under dark conditions) on MB concentration are compared in Fig. 4b. At  $\text{pH} = 5$  and 7, a same low MB discoloration yield of 26–29 % is observed under irradiation conditions. Also, MB appears to be quite stable in stronger alkaline conditions at  $\text{pH} = 9$  in the absence of illumination, which is in line with previous notes [18–20], but under irradiation, photolysis at  $\text{pH} = 9$  shows significant discoloration (44 %) after 180 min of illumination. As it is observed, in even stronger alkaline environment of  $\text{pH} = 12$ , MB

**Fig. 3** Optical absorption spectra: **a** wavelength versus absorbance and **b** energy versus absorbance, of  $\text{TiO}_2$  Degussa (P25) nanoparticles, commercial  $\text{WO}_3$  and the synthesized samples after calcination at  $500^\circ\text{C}$  (WA\_500, WB\_500 and WC\_500)

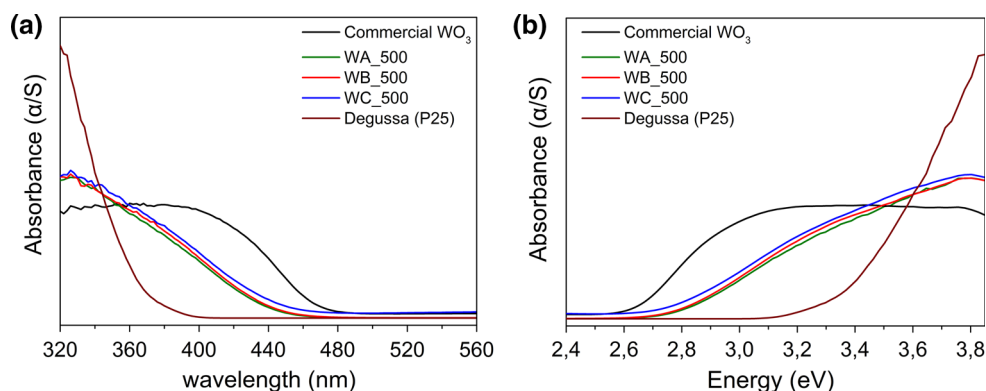
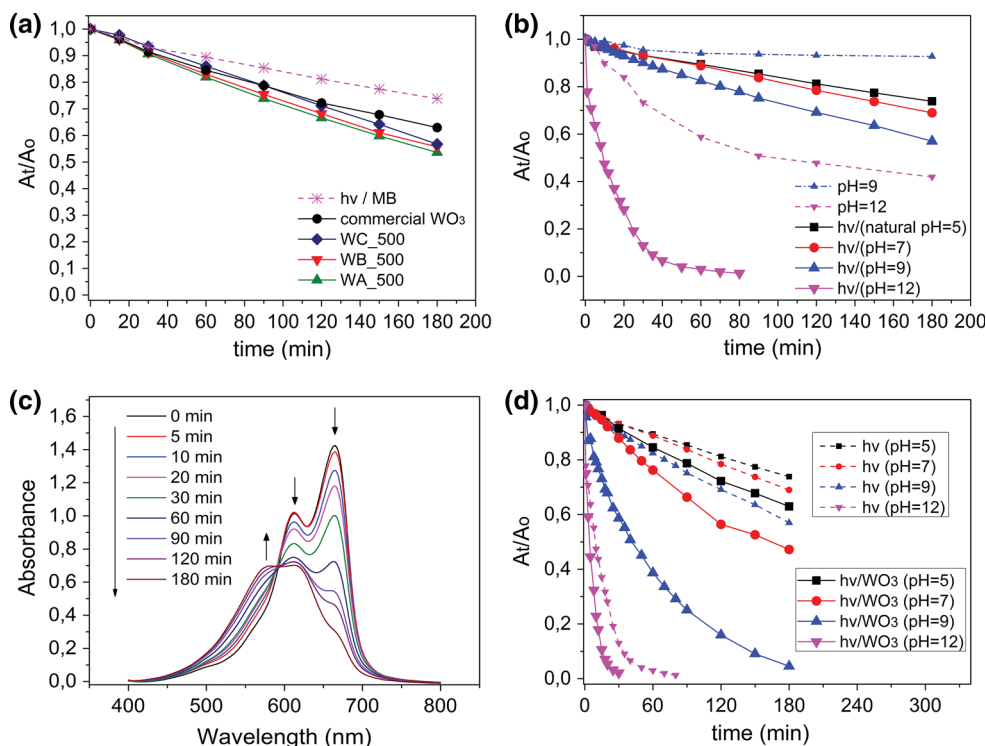
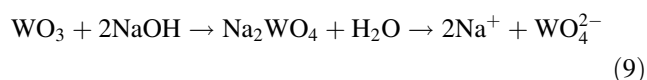


**Fig. 4** **a** Evolution of MB concentration during its photolysis (without catalyst) and photocatalytic MB discoloration with use of commercial  $\text{WO}_3$  and samples WA\_500, WB\_500 and WC\_500 at natural  $\text{pH} \approx 5$ . **b** Effect of NaOH at  $\text{pH} = 9$  and 12 in MB concentration without illumination and catalyst (dashed lines) and photolysis of MB at different pH values. **c** Evolution of the absorption spectra of MB aqueous solution at  $\text{pH} = 12$  over time, under dark conditions and in the absence of catalyst. **d** Comparative diagram of the evolution of MB concentration during photolysis ( $h\nu$ ) at various pH values and the respective photocatalytic discoloration using commercial  $\text{WO}_3$  as catalyst ( $h\nu/\text{WO}_3$ ) at the same pH values



concentration decreases ( $\sim 58\%$  yield) even in the absence of illumination, due to the instability of MB at these high pH conditions, as mentioned above. Figure 4c, shows the evolution of absorption spectra of the aqueous MB solution at pH = 12 without illumination. As can be seen, the two maxima of absorbance at 665 and 610 nm are falling over time, while the maximum at 580 nm is rising, indicating the conversion of MB to MVB. When irradiated, the alkaline aqueous MB solution at pH = 12 shows strong photochemical discoloration efficiency, with almost complete bleaching of the solution (98 %) in 80 min of irradiation time.

The effect of pH on photocatalytic discoloration of the MB solutions using commercial  $\text{WO}_3$  as photocatalyst was also investigated, and the data compared to that of simple photolysis at the various pH values are shown in Fig. 4d. At pH values of 5 (natural pH) and pH 7, the photocatalytic discoloration yields were relatively small (37 and 53 %, respectively) after 180 min of irradiation, although the discoloration efficiencies were enhanced compared to that of simple photolysis at the same pH values. At pH = 9, the use of commercial  $\text{WO}_3$  as catalyst increased the discoloration yield to 96 % after 180 min of irradiation time, showing significant enhancement compared to the discoloration efficiency of simple photolysis at pH 9. The best result for photocatalytic discoloration of MB was obtained at pH 12 (98 % discoloration) after 30 min of irradiation, indicating a faster discoloration efficiency compared to that of simple photolysis at the same pH ( $\sim 98\%$  after 80 min of irradiation). However, in aqueous solutions of pH > 9, MB decomposes slowly even without light irradiation as mentioned above and also  $\text{WO}_3$  dissolves into  $\text{WO}_4^{2-}$  anions as referred to [21] according to the following reaction:



thus making it very difficult to recover the catalyst and ensure steady experimental conditions in order to evaluate and compare the photocatalytic activities of the samples. For this reason, pH 9 was chosen as the optimum pH value, because both MB and  $\text{WO}_3$  appear to be stable under these alkaline conditions and so be ensured that the enhanced MB discoloration is coming only from photocatalytic reactions.

The most possible reason for the different reaction yields at different pH values may be correlated to the generation of active hydroxyl radicals ( $\bullet\text{OH}$ ). Based on the photocatalytic mechanism, the active  $\bullet\text{OH}$  radicals are produced on the surface of the catalyst by the reaction of photogenerated valence band holes ( $h_{\text{vb}}^+$ ) and adsorbed hydroxyl anions ( $\text{OH}^-$ ).  $\text{WO}_3$  has an  $h_{\text{vb}}^+$  potential of about

+3.1 eV that is capable of oxidizing  $\text{OH}^-$  to active  $\bullet\text{OH}$  [22] which are the primary oxidizing species in the photocatalytic oxidation processes. Therefore, the increase in solution pH corresponds to the increase in  $\text{OH}^-$  concentration and thus the increased photocatalytic generation of active hydroxyl radicals from the surface of  $\text{WO}_3$  that enhance the discoloration efficiency of MB.

Figure 5a shows the data corresponding to the photocatalytic discoloration of MB at pH 9 when the different synthesized  $\text{WO}_3$  samples were used as photocatalysts. For comparison, the photocatalytic discoloration of MB over  $\text{TiO}_2$  Degussa (P25) nanoparticles is also shown in Fig. 5a. Although all samples exhibited enhanced discoloration efficiencies compared to simple photolysis at pH 9 and bleached the dye solutions, differences were observed among them regarding their discoloration reaction rates (see Fig. 5b; Table 2). The best photocatalytic activities, close to that of Degussa (98 % discoloration after 60 min of irradiation time), were observed by the samples WA\_500 and WB\_500 with MB discoloration efficiencies over 95 % after 60 and 90 min of light irradiation, respectively (see Fig. 5a), showing higher photocatalytic reaction rates of 0.057 and 0.033  $\text{min}^{-1}$  (see Table 2) which suggest that the reactions proceed at a faster rate over these materials. On the contrary, samples WC\_500 and commercial  $\text{WO}_3$  both showed the same lower photocatalytic reaction rate ( $\sim 0.016 \text{ min}^{-1}$ ) as shown in Table 2, but high discoloration efficiencies nevertheless, over 95 % after 180 min of irradiation. By taking into account the average crystallite size, the morphology and the BET surface area of the samples, the highest photocatalytic activities were observed from the samples WA\_500 and WB\_500, which have smaller average crystallite sizes, more porous morphologies with smaller particles and higher surface areas. On the other hand, the more crystalline samples WC\_500 and commercial  $\text{WO}_3$  showed decreased discoloration reaction rates that can be possibly attributed to their smaller BET surface ( $\sim 3\text{--}4$  times smaller than that of WA\_500 and WB\_500) and their larger grain size and average crystallite size. According to the mechanism discussed before, we suggest that the increased photocatalytic performances observed in samples WA\_500 and WB\_500 are possibly related to their smaller average crystallite size and particle size, which minimize the distance that photogenerated electrons and holes need to reach the solid/liquid interface. Also this effect, combined with the existence of more active sites on the surface of these  $\text{WO}_3$  samples with higher BET surfaces and more porous morphologies, probably leads to a faster and greater direct production of  $\bullet\text{OH}$  at pH = 9, resulting in faster discoloration rates of the MB solutions and also suggesting that  $\bullet\text{OH}$  are the primary oxidizing species in this photocatalytic oxidation process.

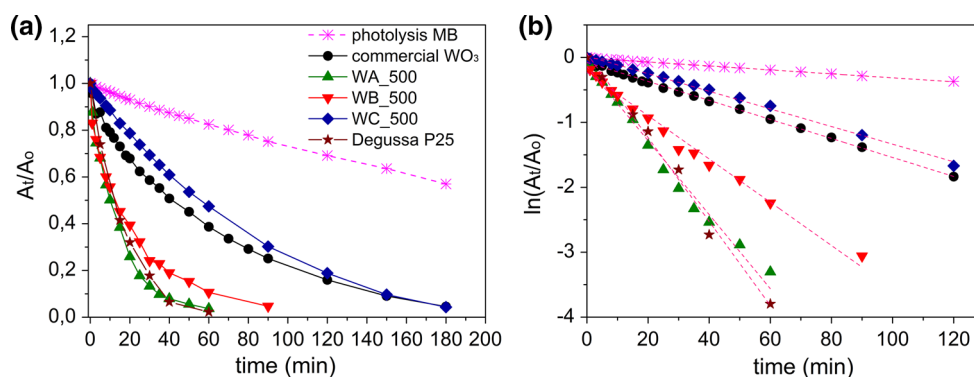


**Fig. 5** **a** Evolution of methylene blue (MB) concentration during its photocatalytic discoloration by the different  $\text{WO}_3$  samples at reaction pH 9 and by  $\text{TiO}_2$  Degussa (P25) nanoparticles. **b** The corresponding pseudo-first-order (red dashed lines are fit to the data) photodiscoloration of MB catalyzed by the different  $\text{WO}_3$  samples and Degussa (P25). Reaction

conditions: 20 mg/l methylene blue, 2 g/l  $\text{WO}_3$  catalyst, 20 °C, reaction pH 9, NUV–visible light irradiation ( $\lambda \geq 300$  nm). The photocatalytic discoloration of MB over  $\text{TiO}_2$  nanoparticles was performed at natural pH ( $\approx 5$ ), using 0.2 g/l catalyst and under NUV–visible light irradiation ( $\lambda \geq 300$  nm) (Color figure online)

**Table 2** Photocatalytic discoloration rate constants of methylene blue in aqueous suspensions of commercial  $\text{WO}_3$  and of the prepared samples WA\_500, WB\_500 and WC\_500 at pH 9 and of  $\text{TiO}_2$  Degussa P25 nanoparticles

Sample	Discoloration rate $k$ ( $\text{min}^{-1}$ )
Commercial $\text{WO}_3$	0.016
WA_500 <sup>a</sup>	0.057
WB_500 <sup>a</sup>	0.033
WC_500 <sup>a</sup>	0.016
$\text{TiO}_2$ Degussa (P25) <sup>b</sup>	0.059

<sup>a</sup> Reaction conditions: 20 mg/l methylene blue, 2 g/l catalyst, 20 °C, reaction pH 9, NUV–visible light irradiation ( $\lambda \geq 300$  nm)

<sup>b</sup> Reaction conditions: 20 mg/l methylene blue, 0.2 g/l Degussa (P25), 20 °C, reaction pH 5 (natural pH), NUV–visible light irradiation ( $\lambda \geq 300$  nm)

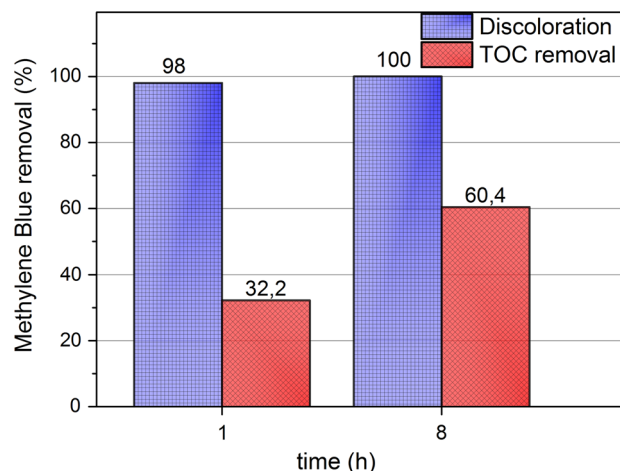


**Fig. 6** Photocatalytic removal of MB according to discoloration and TOC in the presence of WA\_500 catalyst after 1 and 8 h NUV–visible light irradiation. Experimental conditions: initial MB concentration 20 mg/l, catalyst concentration 2 g/l, 20 °C, reaction pH 9

### 3.5 Mineralization

It is well known that complete discoloration of MB does not mean that the dye is completely mineralized into  $\text{CO}_2$  and  $\text{H}_2\text{O}$ . Hence, it is also necessary to investigate the mineralization process. TOC values have been related to the total concentration of organic compounds in the solution and the decrease in TOC reflects the degree of mineralization at the end of the photocatalytic process. Mineralization of MB was studied by monitoring TOC loss in the dye solution.

The TOC removal and discoloration efficiencies via photocatalytic degradation of MB were examined with the use of sample WA\_500 that presented the best discoloration efficiency. The obtained results in experimental conditions of pH 9 under NUV–visible light irradiation are

shown in Fig. 6. After 1 h of irradiation, the dye solution was almost completely bleached (98 % discoloration) but the removal of TOC reached only 32 %, suggesting the formation of intermediate products, which underwent further photocatalytic oxidation as can be seen by the result after 8 h of irradiation (60 % TOC removal). These slowly decreasing TOC values after 1 and 8 h of irradiation time show that the mineralization of MB does not immediately follow the discoloration of the dye solution. At the beginning, the observed discoloration most probably occurs because MB molecules are primarily decomposed to lower molecular weight intermediate compounds that still contribute to the TOC of the solution. These intermediate

products seem to undergo further oxidation but with a much slower rate, indicating that total oxidation or complete mineralization of MB is a very slow process.

## 4 Conclusions

WO<sub>3</sub> catalytic powders were successfully synthesized from tungstic acid and sodium tungstate precursors by simple sol–gel, acid precipitation and low-temperature hydrothermal methods. The resulting samples consisted of nanoparticles with different morphologies and structural properties such as average crystallite size and surface area. The obtained materials were used as photocatalysts for the discoloration of MB aqueous solutions under NUV/visible light irradiation. The role of reaction pH was investigated in a variety of pH values (5, 7, 9 and 12), and experimental results revealed that an alkaline environment was highly favorable for efficient discoloration of MB using WO<sub>3</sub> as photocatalyst, indicating that •OH seem to be the primary oxidizing species in this photocatalytic oxidation process. The as-synthesized catalysts exhibited high photocatalytic efficiency in the discoloration of MB solutions at pH 9, and the samples with smaller average crystallite size, more porous morphology with smaller particle size and higher BET surfaces showed the highest photocatalytic activity. Finally, TOC experiments revealed that mineralization of MB is a much slower process and does not follow the discoloration pattern, suggesting that MB primarily decomposes to intermediate compounds that contribute to the TOC of the solution.

**Acknowledgments** This project is implemented through the Operational Program “Education and Lifelong Learning,” Action Archimedes III and is co-financed by the European Union (European Social Fund) and Greek national funds (National Strategic Reference Framework 2007–2013).

## References

1. Tang J, Zou Z, Ye J (2004) Efficient photocatalytic decomposition of organic contaminants over CaBi<sub>2</sub>O<sub>4</sub> under visible-light irradiation. *Angew Chem Int Edition* 43(34):4463–4466. doi:10.1002/anie.200353594
2. Konstantinou IK, Albanis TA (2004) TiO<sub>2</sub>-assisted photocatalytic degradation of azo dyes in aqueous solution: kinetic and mechanistic investigations: a review. *Appl Catal B* 49(1):1–14. doi:10.1016/j.apcatb.2003.11.010
3. Melghit K, Al-Rubaei MS, Al-Amri I (2006) Photodegradation enhancement of Congo red aqueous solution using a mixture of SnO<sub>2</sub>·xH<sub>2</sub>O gel/ZnO powder. *J Photochem Photobiol, A* 181(2–3):137–141. doi:10.1016/j.jphotochem.2005.11.015
4. Mohamed MM, Othman I, Mohamed RM (2007) Synthesis and characterization of MnOx/TiO<sub>2</sub> nanoparticles for photocatalytic oxidation of indigo carmine dye. *J Photochem Photobiol, A* 191(2–3):153–161. doi:10.1016/j.jphotochem.2007.04.017
5. Sayama K, Hayashi H, Arai T, Yanagida M, Gunji T, Sugihara H (2010) Highly active WO<sub>3</sub> semiconductor photocatalyst prepared from amorphous peroxo-tungstic acid for the degradation of various organic compounds. *Appl Catal B* 94(1–2):150–157. doi:10.1016/j.apcatb.2009.11.003
6. Bamwenda GR, Arakawa H (2001) The visible light induced photocatalytic activity of tungsten trioxide powders. *Appl Catal A* 210(1–2):181–191. doi:10.1016/S0926-860X(00)00796-1
7. Cheng XF, Leng WH, Liu DP, Zhang JQ, Cao CN (2007) Enhanced photoelectrocatalytic performance of Zn-doped WO<sub>3</sub> photocatalysts for nitrite ions degradation under visible light. *Chemosphere* 68(10):1976–1984. doi:10.1016/j.chemosphere.2007.02.010
8. Hong SJ, Jun H, Borse PH, Lee JS (2009) Size effects of WO<sub>3</sub> nanocrystals for photooxidation of water in particulate suspension and photoelectrochemical film systems. *Int J Hydrogen Energy* 34(8):3234–3242. doi:10.1016/j.ijhydene.2009.02.006
9. Turchi CS, Ollis DF (1990) Photocatalytic degradation of organic water contaminants: mechanisms involving hydroxyl radical attack. *J Catal* 122(1):178–192. doi:10.1016/0021-9517(90)90269-P
10. Matthews RW, McEvoy SR (1992) Photocatalytic degradation of phenol in the presence of near-UV illuminated titanium dioxide. *J Photochem Photobiol, A* 64(2):231–246. doi:10.1016/1010-6030(92)85110-G
11. Jimenez I, Centeno MA, Scotti R, Morazzoni F, Arbiol J, Cornet A, Morante JR (2004) NH<sub>3</sub> interaction with chromium-doped WO<sub>3</sub> nanocrystalline powders for gas sensing applications. *J Mater Chem* 14(15):2412–2420. doi:10.1039/B400872C
12. Yu J, Qi L (2009) Template-free fabrication of hierarchically flower-like tungsten trioxide assemblies with enhanced visible-light-driven photocatalytic activity. *J Hazard Mater* 169(1–3):221–227. doi:10.1016/j.jhazmat.2009.03.082
13. Song XC, Zheng YF, Yang E, Wang Y (2007) Large-scale hydrothermal synthesis of WO<sub>3</sub> nanowires in the presence of K<sub>2</sub>SO<sub>4</sub>. *Mater Lett* 61(18):3904–3908. doi:10.1016/j.matlet.2006.12.055
14. Brunauer S, Deming LS, Deming WE, Teller E (1940) On a theory of the van der Waals adsorption of gases. *J Am Chem Soc* 62(7):1723–1732. doi:10.1021/ja01864a025
15. Cox P (1992) Transition metal oxides. Clarendon Press, Oxford
16. Adamčíková Lu, Pavlíková K, Ševčík P (2000) The decay of methylene blue in alkaline solution. *React Kinet Catal Lett* 69(1):91–94. doi:10.1023/A:1005696926749
17. Mills A, Hazafy D, Parkinson JA, Tuttle T, Hutchings MG (2009) Comment on “solvent effect on the electronic spectra of azine dyes under alkaline condition”. *J Phys Chem A* 113(34):9575–9576. doi:10.1021/jp9030927
18. Mills A, Hazafy D, Parkinson J, Tuttle T, Hutchings MG (2011) Effect of alkali on methylene blue (C.I. Basic Blue 9) and other thiazine dyes. *Dyes Pigm* 88(2):149–155. doi:10.1016/j.dyepig.2010.05.015
19. Abbott DC (1962) The colorimetric determination of anionic surface-active materials in water. *Analyst* 87(1033):286–293. doi:10.1039/AN9628700286
20. Holmes W, Snyder E (1929) The atmospheric oxidation, or dealkylation, of aqueous solutions of methylene blue. *Biotech Histochem* 4(1):7–10
21. Gupta CK, Mukherjee T (1990) Hydrometallurgy in extraction processes, vol 2. CRC Press, Boca Raton
22. Mills A, Le Hunte S (1997) An overview of semiconductor photocatalysis. *J Photochem Photobiol, A* 108(1):1–35. doi:10.1016/S1010-6030(97)00118-4